

# Multi-wavelength Diameters of Nearby Miras and Semiregulars

M.J. Ireland,\* P.G. Tuthill, T.R. Bedding, J.G. Robertson and A.P. Jacob

*School of Physics, University of Sydney, NSW 2006, Australia*

19 November 2018

## ABSTRACT

We have used optical interferometry to obtain multi-wavelength visibility curves for eight red giants over the wavelength range 650–1000 nm. The observations consist of wavelength-dispersed fringes recorded with MAPPIT (Masked APerture-Plane Interference Telescope) at the 3.9-m Anglo-Australian Telescope. We present results for four Miras (R Car,  $\rho$  Cet, R Hya, R Leo) and four semi-regular variables (R Dor, W Hya, L<sub>2</sub> Pup,  $\gamma$  Cru). All stars except  $\gamma$  Cru show strong variations of angular size with wavelength. A uniform-disk model was found to be a poor fit in most cases, with Gaussian (or other more tapered profiles) preferred. This, together with the fact that most stars showed a systematic increase in apparent size toward the blue and a larger-than-expected linear size, even in the red, all point toward significant scattering by dust in the inner circumstellar environment. Some stars showed evidence for asymmetric brightness profiles, while L<sub>2</sub> Pup required a two-component model, indicating an asymmetrical circumstellar dust shell.

**Key words:** techniques: interferometry – stars: AGB and post-AGB

## 1 INTRODUCTION

Late-type giants have particularly extended atmospheres, which makes it difficult to define a particular value for the stellar diameter (Baschek et al. 1991; Scholz 2001). Even within the narrower context of observed intensity diameters, their complicated center-to-limb brightness profiles and strong dependence on bandpass from absorption in atmospheric layers leaves no simple “continuum diameter” to be measured.

To truly characterise the brightness distribution of a single late-type giant, one would thus like the complete stellar intensity profile at all wavelengths. Since all of these stars pulsate and some show long-term cycle-to-cycle variations in diameter (eg Tuthill et al. 1995), as expected from models (Hofmann et al. 1998), this information must be obtained simultaneously and the observations then repeated at many different pulsation phases.

There is a significant history of multi-wavelength angular diameter measurements of red giants, beginning with Bonneau & Labeyrie (1973). Unfortunately, difficulties in calibration and the availability of only a few selected bandpasses has meant that spectral coverage of apparent diameter measurements has been limited. In this paper, we present simultaneous multi-wavelength measurements of the apparent sizes of 8 giants using aperture masking interferometry. With a maximum baseline of 3.89 m, our visibility data (related to the object intensity profile by the Fourier transform) were able to resolve all the stars in this sample.

## 2 OBSERVATIONS AND DATA REDUCTION

MAPPIT (Masked APerture-Plane Interference Telescope) was an aperture masking system set up at the coudé focus of the Anglo-Australian Telescope (AAT). The pupil of the AAT was re-imaged onto a mask, with starlight subsequently passing through a prism and cylindrical lens. The optical setup resulted in the image formed at the detector having high-resolution spatial information (fringes) in one direction, and a spectrum of the source in the other. Details of the experiment can be found in Bedding et al. (1994), with the only significant change being the replacement of the IPCS detector with a CCD, accompanied by a change in wavelength coverage to the range 650 nm – 1  $\mu$ m. Previous work with this experimental setup can be found in Jacob et al. (2004).

We used MAPPIT to record wavelength-dispersed fringes from each of three masks: two five-hole linear masks with maximum baselines of 3.2 and 3.8 m, and one slit mask that utilised the full 3.89 m aperture of the AAT. Hole/slit widths of 9, 15 and 18 cm, as projected onto the primary mirror, were available. Data from the wider holes/slits were more influenced by atmospheric noise, while the narrower holes/slits had a narrower effective bandpass, greater resistance against atmospheric noise but inevitably lower transmission. The linear nature of the masks results in only a one-dimensional brightness profile being recorded, however an image rotator enabled different orientations on the sky to be sampled.

The data analysed here were collected on the nights of February 8/9, 2001, with selected known parameters for the target stars given in Table 1 and observational parameters presented in Table 2. Seeing on these nights was above average for the AAT, ranging from 0.8 to 1.3 arcsec. A data set for one target star at one position angle consisted of 2–4 sets of 100–200 frames, with identical ob-

\* E-mail: mireland@physics.usyd.edu.au

**Table 1.** Details of the stars presented in this paper. Phases at the time of the MAPPIT observations were estimated from visual observations.

Name	Pulsation phase	Period (d)	<i>Hipparcos</i> Parallax (mas)
R Car	0.35	309	$7.4 \pm 0.8^b$
<i>o</i> Cet	0.34	332	$7.8 \pm 1.1^a$
R Hya	0.62	389	$8.4 \pm 1.0^b$
R Leo	0.91	310	$12.2 \pm 1.4^b$
R Dor	0.83 <sup>c</sup>	332	$17.0 \pm 0.6^b$
W Hya	0.44	361	$12.9 \pm 1.0^b$
L <sub>2</sub> Pup	0.58	140	$16.5 \pm 1.3^a$
$\gamma$ Cru	–	13–16	$37.1 \pm 0.7^a$

<sup>a</sup> Perryman et al. (1997)

<sup>b</sup> *Hipparcos* data reprocessed by Pourbaix et al. (2003) with a revised chromaticity correction and a more stringent criterion for accepting a variability-induced-mover solution.

<sup>c</sup> R Dor has two pulsation periods: see text.

servations of an unresolved or barely-resolved calibrator star. Exposure times ranged from 10 to 40 ms. Calibration of visibility amplitudes was done by dividing the observed squared-visibilitys of the target star by those of the calibrator. The effects of seeing were not identical between source and calibrator star, due to differences of up to 10 degrees in position on the sky, as well as temporal changes in seeing over the approximately 10 minutes required to interleave observations. To account for this in model fitting, a self-consistent scaling factor (generally between 0.8 and 1.2 in  $V^2$ ) was applied, and the error bars compensated for miscalibration by comparing consecutive observations of different calibrator stars. Calibration of the differential phase of the fringes of target stars across the system bandwidth was not possible, due to uncertainties in system dispersion caused primarily by misalignment errors and differing paths of calibrator and target stars through dispersive optics. Thus, the only phase information used was that contained in the closure phases. Errors not included in the following section are a 1% uncertainty in both the wavelength scale and the detector pixel scale.

The calibrators for each target star are given in Table 2. Corrections were made for partially resolved calibrators, where their angular diameters were estimated from the linear diameters given in Dumm & Schild (1998) and their *Hipparcos* parallaxes. This correction was largest for the bright calibrator 2 Cen, with expected angular size 14.7 mas, which was always used in conjunction with other calibrators to minimise errors.

## 2.1 Coherent Averaging

It is well known in long-baseline optical interferometry that in the photon-starved regime, the signal-to-noise ratio of interferometric data depends primarily on the coherent integration time (Quirrenbach et al. 1994). Although aperture masking does not permit fringe tracking, in post-processing one can use estimates of the atmospheric phase offsets between holes to find a phasor multiplier for each complex visibility. This removes the atmospheric phase noise in the fringes, allowing coherent averaging of visibilitys with an associated increase in signal-to-noise (Marson 1997).

To illustrate the benefits of coherent averaging, consider the simple noise model of a single measurement of complex visibility:

$$V_m = V + \sigma(Z_r + iZ_i). \quad (1)$$

Here,  $V$  is the true visibility,  $Z_r$  and  $Z_i$  are independent standard

**Table 2.** Details of the observations presented in this paper. All observations occurred within twenty-four hours of the Julian Date 2451949.5 (February 8/9, 2001). The (L) and (S) designations represent the long (3.8 m) and short (3.2 m) 5-hole masks respectively. Dimensions are as projected onto the primary mirror, and position angles are given as angles North through East.

Name	Calibrators	Mask type	Hole/slit size (cm)	Position angle (°)
R Car	HR 4050	Slit	18	219
<i>o</i> Cet	$\alpha$ Cet	Slit	15	225
<i>o</i> Cet	$\alpha$ Cet	Hole(S)	18	274
R Hya	2 Cen, $\pi$ Hya	Slit	18	72
R Hya	$\gamma$ Hya, $\pi$ Hya	Slit	18	123
R Leo	$\alpha$ Leo	Slit	9	209
R Leo	$\alpha$ Leo	Slit	9	305
R Leo	$\alpha$ Leo	Hole(S)	15	280
R Leo	$\alpha$ Leo	Hole(S)	15	276
R Dor	$\gamma$ Ret	Hole(S)	18	175
R Dor	$\gamma$ Ret	Hole(S)	18	260
W Hya	$\theta$ Cen	Slit	18	252
W Hya	2 Cen, $\gamma$ Hya, $\pi$ Hya	Slit	18	120
L <sub>2</sub> Pup	$\pi$ Pup	Hole(S)	18	178
L <sub>2</sub> Pup	$\pi$ Pup	Slit	9	209
$\gamma$ Cru	$\alpha^1$ Cru	Hole(L)	9	87

normal distributions and  $\sigma$  represents the noise in a single measurement. For MAPPIT data,  $\sigma$  was often dominated by CCD readout noise. When fringe power, or square visibility modulus is averaged, the resultant incoherently averaged signal-to-noise in  $|V|^2$  is:

$$SN_I = \frac{N_f |V|^2}{2\sigma \sqrt{N_f \sigma^2 + N_f |V|^2}}, \quad (2)$$

where  $N_f$  is the number frames of data with other symbols as before. If coherent averaging is used, the complex visibilitys are averaged and the resultant coherently averaged signal-to-noise is:

$$SN_C = \frac{N_f^2 |V|^2}{2N_f \sigma \sqrt{\sigma^2 + N_f |V|^2}}. \quad (3)$$

In the low signal-to-noise regime, coherent averaging gives a maximum increase in signal-to-noise of  $\sqrt{N_f}$  for  $|V|/\sigma \ll 1$ . For example, this increase in signal-to-noise is as large as 20 for 400 frames of data.

It was possible to estimate the phase offsets between holes for MAPPIT data taken with a hole mask by using a combination of baseline (or phase) bootstrapping and wavelength bootstrapping (see, for example, Armstrong et al. 1998). For coherent averaging to work without the possibility of miscalibration errors, these phase offsets needed to be estimated to an accuracy of much better than 1 radian. This in turn meant that the single-frame signal-to-noise had to be  $\gg 1$  for more visibilitys than the number of atmospheric degrees of freedom. This condition was certainly met in the case of the stars considered here, which had high signal-to-noise for short baselines in pseudo-continuum bands. Estimating the phase offsets in a holistic way (rather than simply choosing a few short baselines and wavelengths from which to bootstrap) required a knowledge of the closure phases at all wavelengths, as well as differential phase offsets between wavelength channels. This knowledge was developed iteratively by starting with a symmetrical model, solving for the the phase offsets for each frame of data, coherently averaging the complex visibilitys, and then producing a new model.

This process is similar to spectral line self-calibration as used

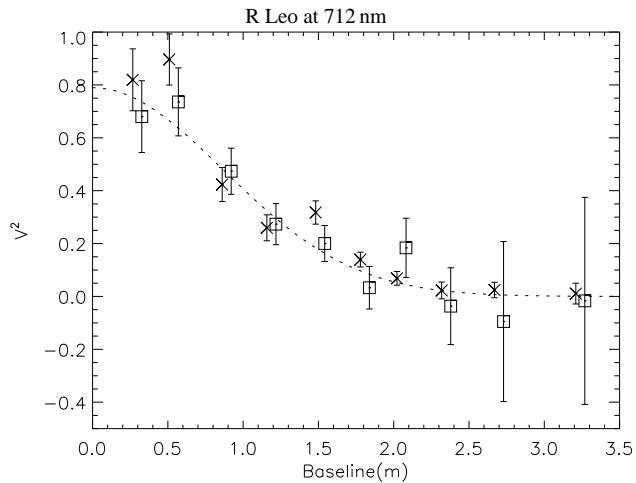


**Figure 1.** A square-visibility curve for R Leo in a single wavelength channel, obtained by dividing the square visibilities of R Leo by those of its calibrator star,  $\alpha$ -Leo. Crosses represent coherently processed data, squares represent conventionally processed (integrated  $V^2$ ) data, and the dotted line is the best fit Gaussian.

in radio astronomy (Taylor et al. 1999), but with a few key differences. The complex telescope gains as used in radio astronomy here become phasors of the form  $e^{2\pi i l_j / \lambda_k}$ , where  $\lambda_k$  is the wavelength of spectral channel  $k$ , and  $l_j$  is an optical path offset for the  $j$ th hole. This replacement of phases  $\phi_j$  with delays  $l_j$  was required because of the large total bandwidth of MAPPIT in combination with atmospherically induced delay errors of up to several microns. Also, no information could be gained from the time dependence of atmospheric delays because there was no correlation between delays in successive frames of data. This is easily explained by the large CCD readout times for MAPPIT (10–40 ms exposures and 650 ms readout time). Lastly, the self-calibration step of regularisation in the image plane was not done as part of our coherent processing, because the reason for self-calibration was to increase signal-to-noise on a self-consistent set of visibilities and closure phases, rather than to form an image.

The final results of coherent averaging are illustrated in Figure 1, using R Leo as an example. It can be seen that the errors in squared visibility are slightly reduced on short baselines, due to MAPPIT’s wavelength bootstrapping ability, and are greatly reduced for the longest baselines, due to both wavelength and baseline bootstrapping. Coherent averaging was used in the processing of all data taken with the 5-hole mask apart from  $\gamma$  Cru, which was in the photon-rich regime for all wavelengths channels. We also note that we found no evidence of any systematic bias when coherently averaged data were compared to incoherently averaged data.

### 3 RESULTS AND DISCUSSION

With up to 40 wavelength channels for each star (note that these are not in general independent; see Section 3.2), the raw visibility data are too extensive to be presented in full. However, an object that we observed at one position angle to be only partially resolved, or one that gave poor signal-to-noise at long baselines, could be adequately fitted by a simple model such as a uniform disk. We thus divided the visibility data into three categories: under-resolved or poor signal-to-noise data, where only an estimate of size could be made; data where an estimate of size could be made and constraints

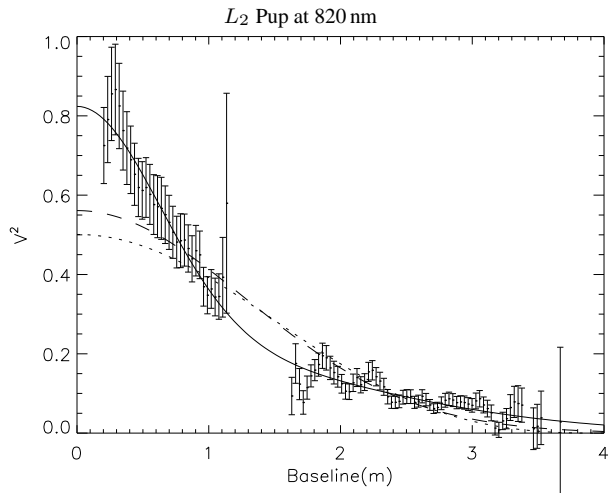


**Figure 2.** The error bars represent calibrated  $V^2$  from  $L_2$  Pup slit data. The gap in  $V^2$  at the shortest baselines is due to the difficulty in calibration as these baselines are highly seeing dependent. The gap between 1.2 and 1.6 m is due to the large central obstruction in the AAT preventing sampling of these baselines. The dashed line is the best single-component Gaussian fit and the dotted line the best uniform disk fit. The solid line is a two-component Gaussian fit with FWHMs  $25 \pm 2$  mas and  $76 \pm 6$  mas, with the smaller component containing  $53 \pm 5\%$  of the flux. Other models with a central bright object and extended flux could also fit the data.

could be placed on the functional form of the brightness profile; and data with high signal-to-noise, where more free parameters were required.

#### 3.1 Rejection of Uniform Disk Model

The model of a uniformly illuminated disk has often been the first choice when fitting to interferometric data. However, this model can be rejected for much of the data presented here. The most striking example of a star that does not match the uniform-disk model is  $L_2$  Pup. For this star, a two-component Gaussian was the simplest model that fitted the data, as shown in Figure 2.

For W Hya, R Dor,  $\alpha$  Cet and R Leo, there were certain wavelength bands where the uniform disk model could be rejected at a  $2\sigma$  level, as given in Table 3. An example visibility curve is given in Figure 3. This kind of profile is indicative of an intensity profile with broad wings. With the exception of the coherently processed data for R Dor and R Leo in strong absorption bands, a Gaussian brightness profile gave a reasonable fit to all visibilities at all wavelengths. There were no data sets where the uniform disk profile was preferred over the Gaussian. We note, however, that many stars were under-resolved at certain wavelengths, especially in near-continuum bands, and many alternative functional forms for the brightness profile (for example, fully-darkened disks) might also fit as well as the Gaussian. For a discussion of this, see Scholz (2003). In the partially-resolved case, one can multiply by a factor of 1.6 to get an equivalent uniform disk diameter from a Gaussian FWHM. In this case, for a bounded intensity distribution, MAPPIT is only capable of measuring the curvature of the  $V^2$  versus baseline curve near the origin, which corresponds to the second moment of the intensity distribution. With all this in mind, the word ‘diameter’ will be used to describe MAPPIT data in the following sections with the meaning of Gaussian FWHM fitted to available baselines. To simplify model fitting, data at baselines beyond where  $V^2$  first fell below 0.01 were ignored.

**Table 3.** Summary of visibility curve constraints for sample stars. With the exception of  $L_2$  Pup, a Gaussian disk model provided a good fit to  $V^2$  in regions where the uniform disk was rejected.

Name	Uniform disk rejection range (nm)	Evidence for Asymmetries?
$\alpha$ Cet	730–850	No
R Hya	—	No
$\gamma$ Cru	—	No
R Car	—	No
R Leo	735–830	Yes
R Dor	720–900	Yes
W Hya	720–900	No
$L_2$ Pup	All (680–920)	Yes

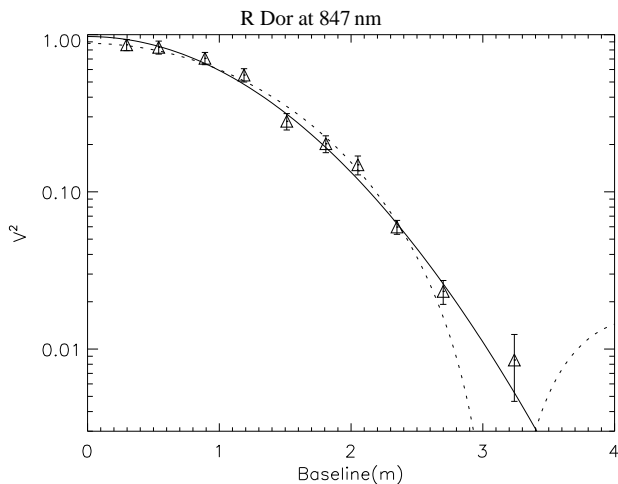


**Figure 3.** Incoherently processed visibilities on a logarithmic scale for R Dor at 847 nm, a uniform disk model (dotted line) with a reduced  $\chi^2$  of 2.19 and a Gaussian disk model (solid line) with a reduced  $\chi^2$  of 1.01. Nearby wavelength channels have similar visibility curves.

### 3.2 Wavelength Dependent Diameters

Given that we have now chosen to fit a single Gaussian profile where possible (i.e., for all stars except  $L_2$  Pup), the visibility data can be distilled to give a plot of the FWHM of the Gaussian profile versus wavelength. Such plots are presented in Figures 4–12. The measured spectrum is overlaid as a dashed line (uncorrected for atmospheric absorption, and in arbitrary units) allowing the position of the absorption bands to be seen clearly and registered against variations in the apparent size. The spectral bandpass of wavelength channels is given as a solid line of arbitrary height, (appearing as a trapezoid to the lower right). The wavelength scale has been plotted in a non-linear fashion so that the size and shape of this spectral bandpass remains the same for all wavelengths. Note that for the narrow holes/slit (for example, in Figure 4) each wavelength channel is nearly independent from its neighbors. Although the MAPPIT instrument was sensitive to wavelengths between about 660 nm and 1020 nm, fits are often not plotted at the shortest wavelengths when the signal-to-noise ratio was too low to give a good fit. Data at wavelengths longer than 940 nm are not plotted whenever intermittent vignetting caused problems with calibration. Results and discussion for individual stars are given below. For a recent review of previous observations of many of these stars, see Scholz (2003).

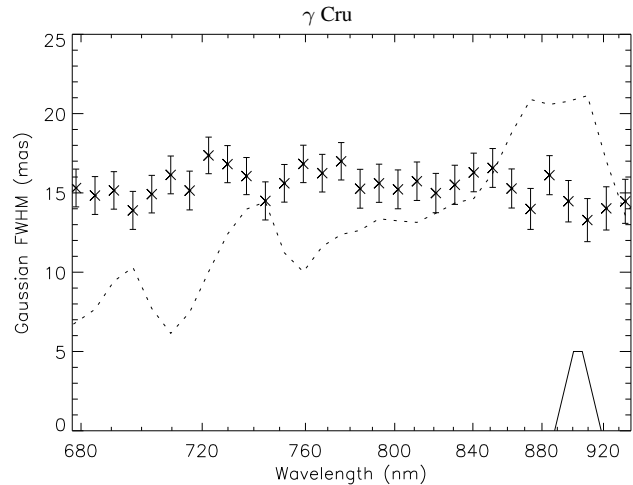


**Figure 4.** FWHM for  $\gamma$  Cru of best-fitting Gaussian disk model as a function of observing wavelength for  $\gamma$  Cru. The over-plotted dashed line gives the spectrum of the star (arbitrary units, not corrected for atmospheric absorption), illustrating for example the well-known TiO absorption features at 710 and 760 nm. The trapezoidal solid line to the lower right shows the spectral bandpass.

#### 3.2.1 $\gamma$ Cru

$\gamma$  Cru is the closest M giant, with spectral type M3.5. Radial velocity observations by Cummings (1999) indicate a pulsation period of 13–16 d, and it is probably on the RGB rather than the AGB (Kiss & Bedding 2003). As can be seen from Figure 4, the variation of angular diameter with wavelength is not statistically significant. Furthermore, the star is barely resolved, so it is meaningful to quote an equivalent mean uniform disk diameter of  $25 \pm 2$  mas. This agrees with a preliminary diameter at  $2.2 \mu\text{m}$  from the VLTI of  $24.7 \pm 0.35$  mas (Glindemann et al. 2001). The MAPPIT diameter should be viewed cautiously, however, as the calibrator,  $\alpha^1$  Cru, is a single-lined spectroscopic binary. If the secondary in this system is of near-equal brightness, then the MAPPIT result could be biased by as much as 4 mas using the orbit from Thackeray & Wegner (1980), giving a corrected angular diameter as high as 29 mas. However, this is unlikely, as both the brightness ratio and the orbital parameters would have to be ‘unlucky’.

We may compare our measured diameter with expectations from the recently calibrated effective temperature scales of late type stars which may be found in van Belle (1999) or Dumm & Schild (1998). Both give  $R_* = 84R_\odot$  with an error of approximately 8% due to the natural dispersion in the relationship. Taking the *Hipparcos* parallax from Table 1 gives an expected diameter of  $28.9 \pm 2.4$  mas, in agreement with our measurement.

#### 3.2.2 $\alpha$ Cet

There are numerous measurements of the diameter of  $\alpha$  Cet in the literature, with the smallest Gaussian FWHM being 12.5 mas in the *J* Band (Ireland et al. 2004). Previous data from the William Herschel Telescope (WHT) show excellent agreement with the MAPPIT data, as shown in Figure 5, although the WHT experiment also measured long-term variations in the diameter of  $\alpha$  Cet in their 700 nm and 710 nm filters (Tuthill et al. 1995). Two clear features in Figure 5 are the increase in apparent size in the absorption bands around 710 and 790 nm by a factor of approximately 1.6 relative to the nearby continuum, and an overall increase in apparent size

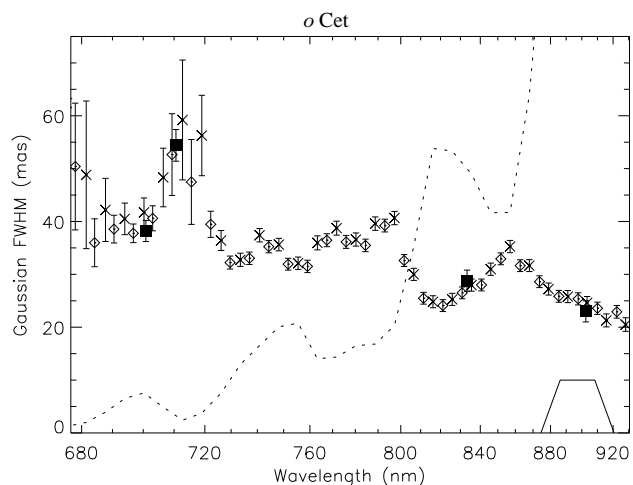


**Figure 5.** Same as Figure 4, but for *o* Cet. Crosses and diamonds are separate MAPPIT runs at the same position angle, at a pulsation phase of 0.38. These data were taken with a slit mask; additional data taken with a 5-hole mask (not presented) had lower signal-to-noise but were also consistent with the slit data. The four squares are 1993 data from the WHT (Tuthill et al. 1995), at a pulsation phase of 0.48.

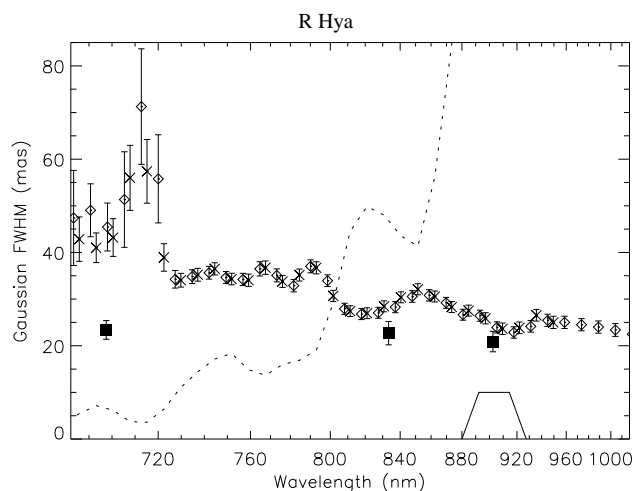


**Figure 6.** Same as Figure 4, but for R Hya. Crosses and diamonds are separate MAPPIT runs at position angles of  $72^\circ$  and  $123^\circ$ . Again, the three squares are 1993 WHT data. The pulsation phases are 0.28 and 0.62 for the WHT and MAPPIT data, respectively.

toward the blue, with a 1.8 times increase in apparent diameter at 700 nm relative to 920 nm.

### 3.2.3 R Hya

Figure 6 again compares MAPPIT wavelength-dependent diameters to results from the WHT experiment (Haniff et al. 1995). The large difference in these data sets could be due to the difference in pulsation phase and/or long term variability in size between the two observations. Note that although the apparent size of this star changes less than *o* Cet in TiO absorption bands, there is a larger increase in apparent diameter toward the blue (about a factor of 2.0 between 700 nm and 920 nm).

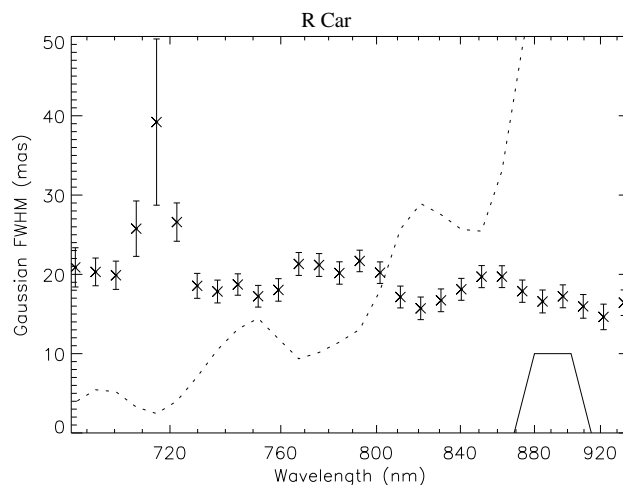


**Figure 7.** Same as Figure 4, but for R Car.

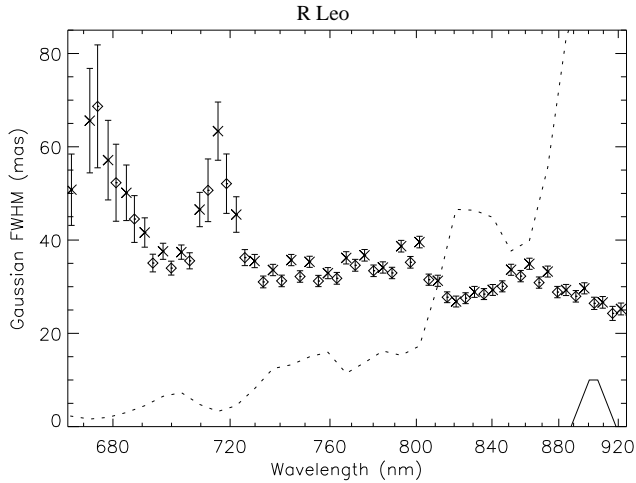
### 3.2.4 R Car

Figure 7 represents the first published angular diameter measurement for this star. Although the signal-to-noise is lower than for the other stars, the increase in apparent size in the 712 nm TiO band is clear, as is the relatively small increase in apparent size toward the blue (roughly a factor of 1.4 between 700 nm and 920 nm).

### 3.2.5 R Leo

The two diameter vs. wavelength plots for R Leo, Figures 8 and 9 show data from a slit mask and a hole mask respectively. Although these show some differences in detail, as we explain below, the two curves are consistent within errors. The higher spectral resolution of the narrow slit enabled a larger increase in apparent diameter to be seen in the 712 nm absorption band (roughly a factor of 1.9 larger than nearby continuum). For all other Mira-like stars observed here with wider slits/holes, the 712 nm absorption band was slightly contaminated by neighboring continuum, lessening the change in the apparent size. Although the two position angles appear to give different sizes in the wavelength range 730–850 nm, note that the data points at neighboring wavelengths are not independent because they are equally affected by calibration errors caused by changes in seeing. For the data taken with the 5-hole mask, the smaller apparent change in diameter in the 712 nm TiO band is due to two reasons: the effective filter profile was wider than the slit mask, and the Gaussian profile was a poor fit to the 670 and 712 nm data. This poor fit was due to the higher signal-to-noise on the longer baselines enabled by coherent processing, which gave a two-component-like fit. The slit data had lower long-baseline signal-to-noise, and were thus sensitive only to the larger component. The brightness profile reconstructions in Section 3.3 give a qualitative picture of this two-component-like appearance.

Hofmann et al. (2001) measured the azimuthally averaged Gaussian FWHM for R Leo, at a pulsation phase of 0.2, to be  $30.5 \pm 1.5$  mas and  $34.6 \pm 1.6$  mas at wavelengths of 754 and 781 nm respectively, consistent within errors with the MAPPIT result. Their measured FWHM of  $23.6 \pm 2.6$  mas at 1045 nm is consistent with the MAPPIT result at 920 nm. Burns et al. (1998) measured the diameter of R Leo at 830 and 940 nm increasing between phases of 0.1 and 0.6, with measurements at a phase of 0.2 being most consistent with the MAPPIT diameters (at phase 0.91).



**Figure 8.** Same as Figure 4, but for R Leo. Crosses and diamonds represent data at position angles of  $305^\circ$  and  $209^\circ$ , respectively, using a slit mask.

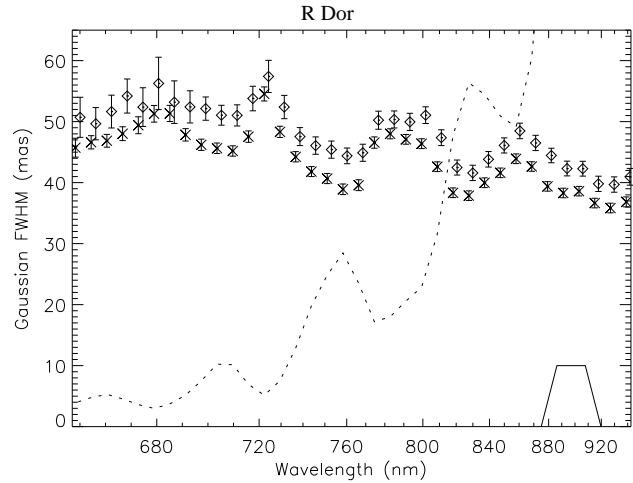


**Figure 10.** Same as Figure 4, but for R Dor. Crosses and diamonds represent data at position angles of  $175^\circ$  and  $260^\circ$  respectively.

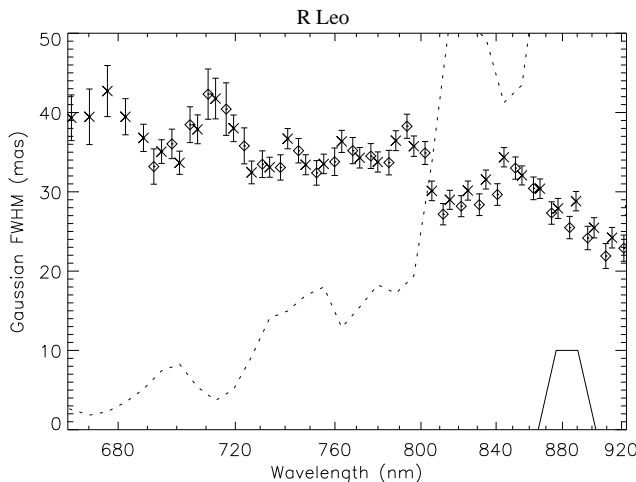


**Figure 9.** Same as Figure 8, but for a hole mask. Crosses and diamonds represent data at position angles of  $276^\circ$  and  $280^\circ$ , respectively. The data points in the absorption bands at 670 and 712 nm are not valid, because a Gaussian disk is a poor fit to the data (in Figure 8 signal-to-noise was poor at all baselines greater than 1 m). See section 3.3 for details.

### 3.2.6 R Dor

R Dor is a semi-regular variable with a dominant pulsation period of 332 days, typical of a Mira-like variable, and a secondary pulsation period of 175 days (Bedding et al. 1998). Its diameter has previously been measured by Bedding et al. (1997), whose results at 1250 nm can be converted to a Gaussian FWHM of 36 mas, consistent with the MAPPIT measurements here. The diameter vs. wavelength plot for R Dor shown in Figure 10 is noticeably different from those for other stars shown in this paper. Both the increase in apparent size toward the blue and the variation in apparent size in absorption bands are considerably less than for the large-amplitude Mira stars presented thus far. Furthermore, the data from the two position angles separated by approximately 90 degrees show significantly different apparent sizes. Fortunately, this star is well-resolved and the details of this apparent asymmetry are investigated further in Section 3.3.

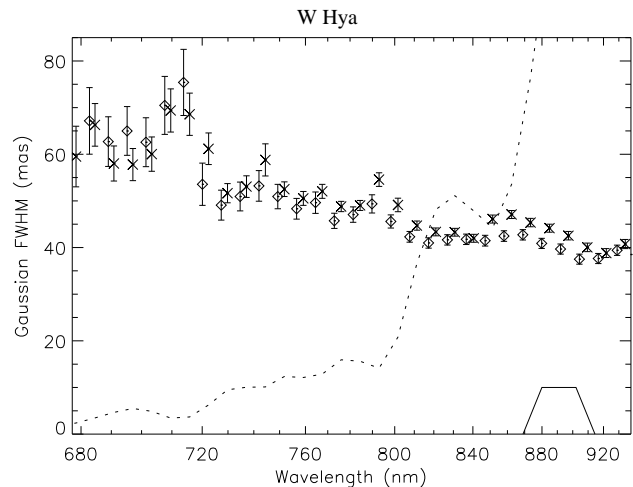


**Figure 11.** Same as Figure 4, but for W Hya. Crosses and diamonds represent data at position angles of  $252^\circ$  and  $120^\circ$  respectively.

### 3.2.7 W Hya

W Hya is also classified as a semi-regular variable, but has only one dominant pulsation period of 361 days and has a visual amplitude of 3 magnitudes, meaning it should be classified as a Mira variable. Its diameter vs. wavelength plot in Figure 11 has less variation of apparent diameter in absorption bands than the other large-amplitude Mira stars presented here, but shows the same strong increase in apparent diameter toward the blue (roughly a factor of 1.6 between 920 and 700 nm). Although there are some signs of asymmetries at the 10% level around 850 nm, these cannot be interpreted further due to the unavailability of phase information, as phase information recovered from slit masks has a low signal-to-noise ratio.

### 3.2.8 L<sub>2</sub> Pup

L<sub>2</sub> Pup is a semi-regular variable with a pulsation period of 140 days and no previous measurements of its diameter. Using the angular size versus  $V - K$  colour relationship for variable stars from van Belle (1999), taking the mean  $K$  magnitude of  $-2.24$  from

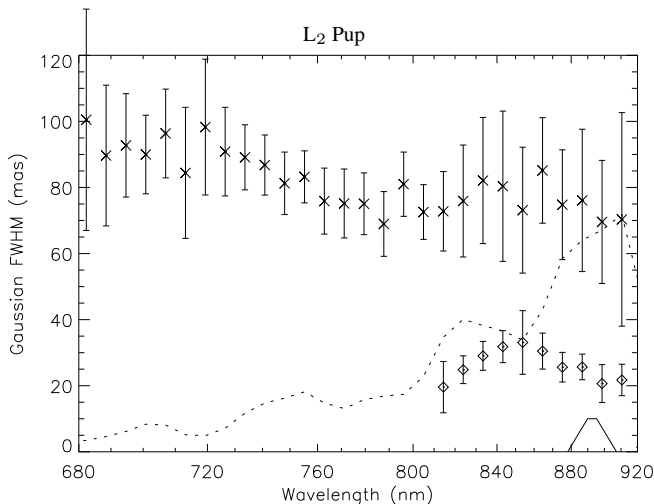


**Figure 12.** Same as Figure 4, but for  $L_2$  Pup, for data taken with a slit mask. Crosses represent the larger of two components in a two-component fit, and diamonds represent the smaller component. Long baseline signal-to-noise was too low at wavelengths shorter than 800 nm for the smaller of the two components to be significantly resolved.

Whitelock et al. (2000) and a  $V$  magnitude of 5.2, the predicted Gaussian FWHM of  $L_2$  Pup is 15 mas. This is consistent with the smaller of the two components shown in Figure 12. The origin of the larger component will be discussed further in Section 3.3.

### 3.2.9 Implications for Mira atmospheres

The five Mira stars share three common features: Firstly, there is an enlargement by up to a factor of 2 in the strongest TiO bands at 712 and 670 nm, when compared to diameters at nearby wavelengths. Contamination by nearby continuum radiation is a significant factor for all these data, except for R Leo data taken with the narrow slit mask. In particular, the “true” apparent enlargement of R Hya and  $\alpha$  Cet in the 710 nm absorption band would roughly be a factor of 2.0 rather than 1.4 and 1.6 as shown above, if a narrower filter were used. This kind of extension is expected from dynamical models such as those investigated in Jacob & Scholz (2002). Note that the maximum extension produced by hydrostatic models is around 30% over the wavelength range considered here (Hofmann & Scholz 1998), demonstrating the need for dynamical models in modeling Mira-like atmospheres.

Secondly, the minimum diameters of these stars are systematically too large for published models. The most extreme dynamical fundamental-mode models from Jacob & Scholz (2002) predict a maximum 920 nm radius of  $340R_{\odot}$  for a short to medium baseline fit to their models, which corresponds to a FWHM of 2.0 AU in Figure 13. This means that three stars in this group are systematically too large for all of those Mira-like models. Hydrostatic models such as those by Bessell et al. (1991) are considerably smaller. Although models that pulsate in the first overtone can explain these larger sizes, they cannot explain the small infra-red sizes observed (for example, see Ireland et al. 2004 or Perrin et al. 1999). It has been pointed out in the model study of Bedding et al. (2001) that scattering by dust in the upper atmosphere of Miras could explain these larger apparent diameters, as well as their two-component or Gaussian-like appearance at wavelengths shorter than 1 micron. Dust was also cited by Hofmann et al. (2001) to explain their observations of large apparent diameters. Danchi et al. (1994) mea-

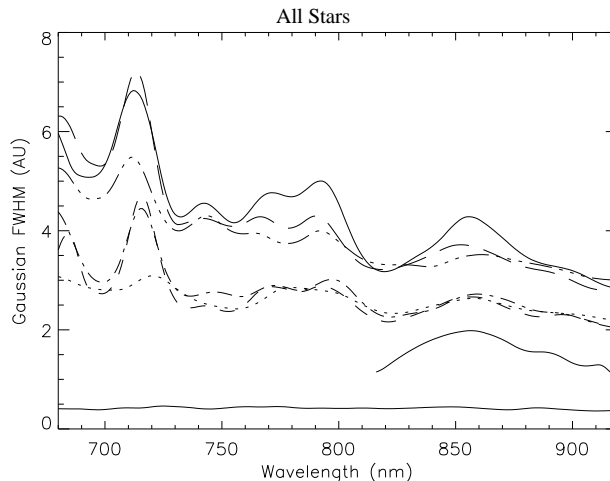


**Figure 13.** Linear size vs. wavelength for all stars in the sample, using their *Hipparcos* parallaxes (given in Table 1). Diameters for different runs on the same star have been averaged together and smoothed. From top to bottom the stars are  $\alpha$  Cet (solid line), R Hya (large dashes), W Hya (triple-dot dashed), R Leo (dot-dashed), R Car (small dashes), R Dor (dotted), the smaller component of  $L_2$  Pup (solid line) and  $\gamma$  Cru (solid line). The larger component of  $L_2$  Pup (not shown) has an average size of 5 AU.

sured the size of the dust shells around several Mira-like stars, and found an inner radius of the dust shell less than 2.7 continuum radii from the star’s centre, and predicted an optical depth (including scattering and absorption) of 0.5 for a 700 nm wavelength. This is enough to explain the larger observed diameters as compared with those expected from dust-free model studies such as Jacob & Scholz (2002).

Finally, there is a trend of increasing apparent size toward the blue, which is not always correlated with an increase in apparent size in TiO bands. W Hya is the most striking example of this, with a large increase in apparent diameter toward the blue but only small changes in apparent diameter in absorption bands. W Hya and R Hya (which also shows a large increase in apparent size toward the blue) are also the stars observed closest to minimum. If scattering by dust is a major contributor to this effect, then this might suggest that significant dust production occurs near minimum.

### 3.3 Asymmetrical Targets

We see asymmetries, as indicated by non-zero closure phases, in the stars R Leo, R Dor and  $L_2$  Pup. The maximum closure phase observed was  $-90^\circ$  at  $5\sigma$  for R Dor. For these stars, which also have reasonable signal-to-noise at visibilities less than 0.1, a simple model diameter does not fully represent the available data. We thus present reconstructed one-dimensional brightness profiles. Data at a variety of position angles would be needed in order to reconstruct a two-dimensional image, but the one-dimensional data still allows quantification of the wavelength-dependent structure in these stars. The one-dimensional profiles were constructed using the Maximum Entropy (MEM) algorithm as described in Wilczek & Drapatz (1985). Each point in the profile can be thought of as the integral of the image flux along an axis perpendicular to the position angle of observation. Flux is scaled so that the peak flux is always 1.0 in order to easily show the difference in the shapes of the flux distributions. The absolute positions of the profiles are also arbitrary, as uncertainties in the dispersion of the opti-

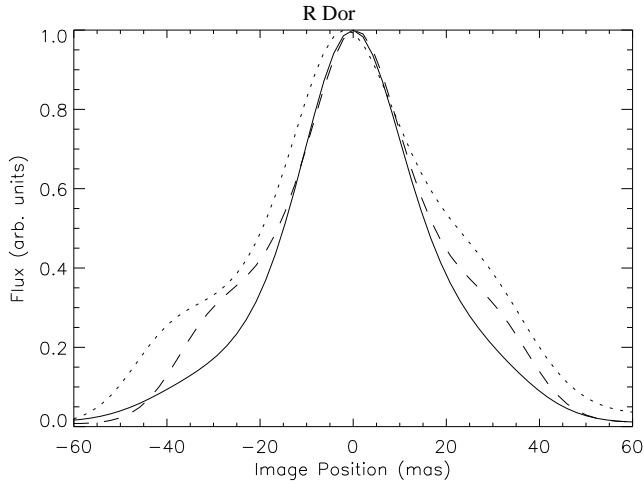


**Figure 14.** MEM reconstructed brightness profiles of R Dor at a position angle of  $175^\circ$ . The solid line is at 750 nm, the dotted line at 712 nm and the dashed line at 700 nm.

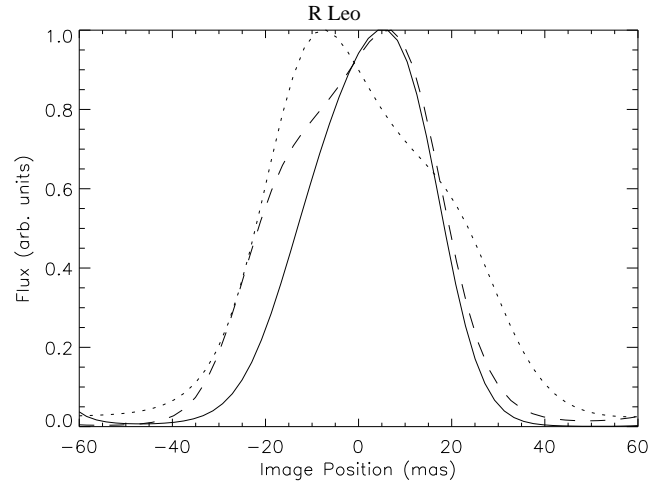


**Figure 17.** MEM reconstructed brightness profiles of R Leo at a position angle of  $276^\circ$ . The solid line is at 815 nm, the dashed line at 700 nm and the dotted line at 712 nm.

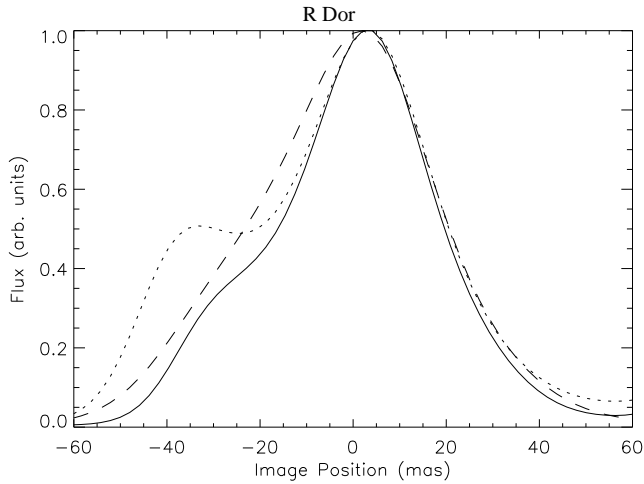


**Figure 15.** The same as Figure 14, but at a position angle of  $260^\circ$ .

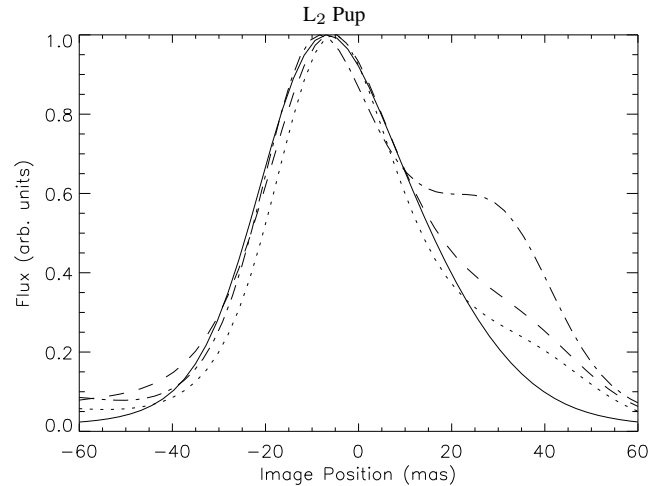


**Figure 18.** MEM reconstructed brightness profiles of L<sub>2</sub> Pup at a position angle of  $178^\circ$ . The solid line is at 850 nm (weak TiO), the dotted line at 820 nm (pseudo-continuum), the dashed line at 790 nm (weak TiO) and the dot-dashed line at 750 nm (pseudo-continuum).

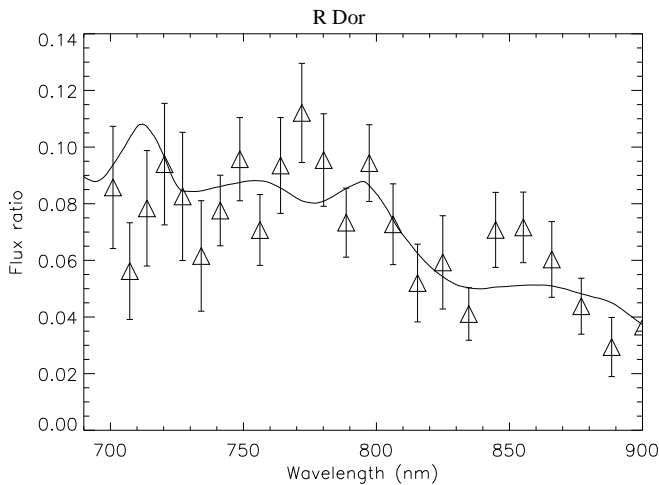


**Figure 16.** The ratio of point source to disk flux for the model of R Dor described in the text, overlaid with a scaled ratio of an M6 to an M8 model spectrum (Fluks et al. 1994).

cal system made differential phase measurements impossible over the full bandwidth.

The three stars presented here have quite different characteristics. The brightness profiles of R Dor in Figures 14 and 15 are dominated by a central Gaussian-like profile with additional features that become stronger in the absorption bands. For the observations at a position angle of  $260^\circ$ , it was possible to model the flux as a central Gaussian disk with FWHM that varied with wavelength, and a point source offset by  $36.2 \pm 0.5$  mas in all wavelength channels. The ratio of the flux in these two components at wavelengths between 700 and 900 nm is given in Figure 16, along with a tentative fit based on a temperature difference between components. It is clear that the point source in the model contributes to more of the total flux toward the blue, however it is not clear whether this is due to a spatial variation in temperature causing a spatial variation in TiO opacity, or from an effect in the inner circumstellar environment such as scattering by dust.

The brightness profiles of R Leo in Figure 17 have opposite

directions of skew in the 712 nm absorption band and the continuum, suggesting that the flux in this band is dominated by one or more non-central bright spots. Quantitative interpretation of this is difficult, because the phase signal is weak, so model-fitting the flux in two components: a central disk and off-centre spot, gives a large error in the relative flux in the two features at all wavelengths. The strength of these asymmetries is similar to that found in earlier work by Tuthill et al. (1999).

The asymmetry in the profiles of L<sub>2</sub> Pup increases toward the blue, as shown in Figure 18. There is no significant increase in the strength of the asymmetrical feature in the weak absorption bands at 790 and 850 nm. The signal-to-noise for shorter wavelengths than those presented here was low, but the trend in the two component fits from section 3.2 was that the central component was contributing relatively less flux toward the blue. We therefore interpret the wide asymmetrical feature as scattering by dust in the circumstellar environment. The large change in the strength of this feature between 750 and 850 nm relative to the central source is indicative of the extent of dust extinction for this star. This extinction had increased by approximately 2 magnitudes in *V* immediately prior to these observations (Bedding et al. 2002).

#### 4 CONCLUSION

Simultaneous spatial and spectral data have been recorded for a sample of eight red giants using the novel cross-dispersed interferometry technique developed by the MAPPIT project. With spectral resolving power  $\lambda/\delta\lambda < 100$  and spatial resolutions sufficient to measure structures  $> 10$  mas in size, it has been possible to recover the angular size distribution as a function of wavelength spanning the R and I-bands for our sample stars. A combination of wavelength and baseline bootstrapping enabled coherent averaging of many data sets, enabling a large increase in the signal-to-noise ratio. With the exception of  $\gamma$  Cru, which had a much earlier spectral type (M3.5) than the rest of the sample, diameters were found to exhibit dramatic changes with wavelength. These diameter excursions occurred both as broad trends with wavelength across the entire band, and in narrow spectral windows. In the latter case, the changes were manifest as enlargements across spectral regions associated with strong TiO absorption, although these were mixed with nearby quasi-continuum layers at the spectral resolutions achieved here, arguing for further work with higher dispersion.

For the Mira variables in the sample, Gaussian-like (or other tapered) radial profiles were found to give a better fit to the data than uniform disk profiles. The prevalence of these Gaussian-like profiles, the increase in apparent size toward the blue as separate from molecular effects and the larger than expected apparent sizes even at 920 nm all point toward the significance of scattering by dust in the inner circumstellar environment affecting interferometric observations at these wavelengths. Non-centro-symmetric elements were detected for 3 stars, which may be explained as thermal or opacity inhomogeneities in the stellar atmosphere or inner circumstellar regions.

The star L<sub>2</sub> Pup was found to be something of a special case, with the visibility data betraying the presence of two resolved components, which we interpret as a stellar disk and a dusty circumstellar envelope. Asymmetries detected in this star raise the interesting possibility of resolved highly clumpy structure as close as the dust condensation radius.

These results are all in accord with the theoretical and obser-

vational picture of pulsating late-M giants which emphasizes the potential for the extended molecular atmosphere to dramatically affect the observed properties of the stars.

#### ACKNOWLEDGMENTS

Visual data for estimating the phases of the MAPPIT observations were supplied by the AFOEV, the VSOLJ and Albert Jones. We thank M. Scholz for many valuable discussions, and the Anglo-Australian Observatory for their support for the duration of the MAPPIT experiment. This research was in part supported by the Australian Research Council and the Deutsche Forschungsgemeinschaft within the linkage project "Red Giants."

#### REFERENCES

- Armstrong, J. T., Mozurkewich, D., Pauls, T. A., & Hajian, A. R., 1998, In *Reasenberg, R. D., ed., Proc. SPIE Vol. 3350, Astronomical Interferometry*, volume 3350, page 461.
- Baschek, B., Scholz, M., & Wehrse, R., 1991, *A&A*, 246, 374.
- Bedding, T. R., Jacob, A. P., Scholz, M., & Wood, P. R., 2001, *MNRAS*, 325, 1487.
- Bedding, T. R., Robertson, J. G., & Marson, R. G., 1994, *A&A*, 290, 340.
- Bedding, T. R., Zijlstra, A. A., Jones, A., & Foster, G., 1998, *MNRAS*, 301, 1073.
- Bedding, T. R., Zijlstra, A. A., Jones, A., Marang, F., Matsuura, M., Retter, A., Whitelock, P. A., & Yamamura, I., 2002, *MNRAS*, 337, 79.
- Bedding, T. R., Zijlstra, A. A., von der Luhe, O., Robertson, J. G., Marson, R. G., Barton, J. R., & Carter, B. S., 1997, *MNRAS*, 286, 957.
- Bessell, M. S., Brett, J. M., Scholz, M., & Wood, P. R., 1991, *A&AS*, 89, 335.
- Bonneau, D., & Labeyrie, A., 1973, *ApJ*, 181, L1.
- Burns, D., Baldwin, J. E., Boysen, R. C., Haniff, C. A., Lawson, P. R., Mackay, C. D., Rogers, J., Scott, T. R., St.-Jacques, D., Warner, P. J., Wilson, D. M. A., & Young, J. S., 1998, *MNRAS*, 297, 462.
- Cummings, I. PhD thesis, Univ. Canterbury, 1999.
- Danchi, W. C., Bester, M., Degiacomi, C. G., Greenhill, L. J., & Townes, C. H., 1994, *AJ*, 107, 1469.
- Dumm, T., & Schild, H., 1998, *New Astronomy*, 3, 137.
- Fluks, M. A., Plez, B., The, P. S., de Winter, D., Westerlund, B. E., & Steenman, H. C., 1994, *A&AS*, 105, 311.
- Glindemann, A., Bauvir, B., van Boekel, R., Corria, F., Delplanck, F., Derie, F., di Folco, E., & Gennai, A. *et al.*, 2001, *The ESO Messenger*, 104, 2.
- Haniff, C. A., Scholz, M., & Tuthill, P. G., 1995, *MNRAS*, 276, 640.
- Hofmann, K.-H., Balega, Y., Scholz, M., & Weigelt, G., 2001, *A&A*, 376, 518.
- Hofmann, K.-H., & Scholz, M., 1998, *A&A*, 335, 637.
- Hofmann, K.-H., Scholz, M., & Wood, P. R., 1998, *A&A*, 339, 846.
- Ireland, M. J., Tuthill, P. G., Bedding, T. R., Robertson, J. G., Jacob, A. P., Monnier, J. D., & Danchi, W. C., 2004, In *Kurtz, D. W., and Pollard, K., eds., Proc. IAU Colloquium 193, Variable stars in the Local Group*. in press.

- Jacob, A. P., Bedding, T. R., Robertson, J. G., Barton, J. R., Haniff, C. A., & Marson, R. G., 2004, MNRAS, pages —. Submitted.
- Jacob, A. P., & Scholz, M., 2002, MNRAS, 336, 1377.
- Kiss, L. L., & Bedding, T. R., 2003, MNRAS, 343, L79.
- Marson, R. *Analysis Techniques for Optical Interferometry: Theory and Practice*. PhD thesis, University of Sydney, 1997.
- Perrin, G., Coudé du Foresto, V., Ridgway, S. T., Mennesson, B., Rulhier, C., Mariotti, J.-M., Traub, W. A., & Lacasse, M. G., 1999, A&A, 345, 221.
- Perryman, M. A. C., Lindegren, L., Kovalevsky, J., Hoeg, E., Bastian, U., Bernacca, P. L., Crézé, M., Donati, F., Grenon, M., van Leeuwen, F., van der Marel, H., Mignard, F., Murray, C. A., Le Poole, R. S., Schrijver, H., Turon, C., Arenou, F., Froeschlé, M., & Petersen, C. S., 1997, A&A, 323, L49.
- Pourbaix, D., Platais, I., Detournay, S., Jorissen, A., Knapp, G., & Makarov, V. V., 2003, A&A, 399, 1167.
- Quirrenbach, A., Mozurkewich, D., Buscher, D. F., Hummel, C. A., & Armstrong, J. T., 1994, A&A, 286, 1019.
- Scholz, M., 2001, MNRAS, 321, 347.
- Scholz, M., 2003, In *Traub, W. A., ed., Proc. of the SPIE, Volume 4838, Interferometry for Optical Astronomy II.*, page 163.
- Taylor, G. B., Carilli, C. L., & Perley, R. A., editors. *Synthesis Imaging in Radio Astronomy II*, 1999.
- Thackeray, A. D., & Wegner, G., 1980, MNRAS, 191, 217.
- Tuthill, P. G., Haniff, C. A., & Baldwin, J. E., 1995, MNRAS, 277, 1541.
- Tuthill, P. G., Haniff, C. A., & Baldwin, J. E., 1999, MNRAS, 306, 353.
- van Belle, G. T., 1999, PASP, 111, 1515.
- Whitelock, P., Marang, F., & Feast, M., 2000, MNRAS, 319, 728.
- Wilczek, R., & Drapatz, S., 1985, A&A, 142, 9.